Radiation and supernovae feedback during the epoch of reionization with EMMA

Nicolas Deparis[1]⋆, Dominique Aubert[1], Pierre Ocvirk[1] and Nicolas Gillet[2]

[1] *Observatoire Astronomique de Strasbourg, CNRS UMR 7550, Universite de Strasbourg, Strasbourg,France*
[2] *Scuola Normale Superiore, Piazza dei Cavalieri 7, I-56126 Pisa, PI, Italy*

ABSTRACT

We aim at investigating the role of stellar feedback in large scale cosmological simulations of reionization, in the regime of kpc resolution. The link between star formation, ionizing sources and supernovae feedback at high redshift is examined using EMMA , a radiative-hydrodynamics (RHD) code with adaptive mesh refinement (AMR). We present a new supernovae feedback model based on kinetic energy injection and compare this model to simple thermal injection scheme. We show that this model is able to regulate star formation on a wide range of halo masses. We compute the average velocity of galactic winds around halos and we show that our feedback model is able to efficiently generate galactic outflows for halos with masses between $10^8 M_\odot$ and $10^{11} M_\odot$. We then investigate the influence of the various feedbacks on the reionization process and show that an increase in the UV escape fraction can compensate for a decreasing star formation rate in our models. As a result different star formation histories can lead to similar evolutions for global reionizations.

Key words: cosmology: dark ages, reionization, first stars - methods: numerical

1 INTRODUCTION

Stellar feedback is a crucial ingredient in the process of galaxy formation. By changing the state of the inter-stellar medium (ISM), stellar feedback introduces a highly nonlinear coupling between the accretion and outflow of gas material in dark matter haloes which is regulating the star formation process in galaxies. Supernovae explode inside star-forming regions and blow away the gas that is needed for the future generation of stars. Therefore, the more efficient is the star formation process, the more efficient is the feedback and the less efficient is the subsequent star formation. These effects are especially important during the epoch of reionization when the star formation process begins. Understanding the star formation process is therefore crucial during this period in order to correctly follow the build-up of the first generation of ionizing sources.

Supernova feedback was introduced in cosmological simulations mainly for two reasons. First it has been implemented to compensate the overcooling problem, leading to galaxies with far larger baryonic masses compared to observed ones. Secondly, supernova feedback was studied to reproduce observed galactic outflows (Veilleux et al. 2005) that have been found to be difficult to obtain in simulations.

Even if supernova feedback has been extensively investigated for more than two decades (starting with Katz (1992); Navarro & White (1993)), its numerical implications are still unclear (see e.g. Rosdahl et al. (2016)). Different kinds of subgrid modelling have been developped for the supernova feedback with different levels of complexity depending of the spatial resolution of the simulations (like e.g. thermal injection where energy is thermally dumped into the gas(Katz 1992), kinetic feedback (Navarro & White 1993; Dubois & Teyssier 2008) where momentum is explicitly transmitted or delayed cooling (Stinson et al. 2006) which differ the effects of cooling to prevent the energy to radiate away). A few projects have been undertaken to compare the feedback implementations (Kimm et al. 2015; Rosdahl et al. 2016), but there is still no consensus about the right way to deal with it in simulations.

In this work, we focus on the reionization epoch and we consider that stars in star-forming galaxies are the main emitters of ionizing photons[1]. It is still unclear how UV radiation can escape the hosting dark matter haloes: the way photons propagate through the gas is highly dependent to the local density which depends on the stellar feedback. Therefore, there is a direct link between star formation, stellar feedback and ionizing sources during the reioniza-

---

⋆ E-mail: nicolas.deparis@astro.unistra.fr

[1] It has been shown recently that accreting black holes in Active Galactic Nuclei (AGNs) could contribute significantly to the UV photon budget (Giallongo et al. 2015; Haardt & Madau 2012; Chardin et al. 2017; D'Aloisio et al. 2016) However, star-forming galaxies are still the main candidates (Bouwens et al. 2015)

tion process. Understanding where and how stars form is primordial to understand which radiative sources dominate the photon budget.

The main difficulty is the underlying multi-scale problem where supernova explosion occur at sub-parsec scale while creating gas outflow at scales up to several tens of kiloparsecs and Reionization occurs on tens of Mpc scales. This is especially hard to tackle in simulations of the Reionization process where we ideally want to simulate a very large volume to correctly sample the cosmic variance : Iliev et al. (2014) have indeed shown that a volume of 50-100 cMpc is needed to correctly follow the reionization process. Considering such volumes and the current super-computing facilities, simulations are still unable to resolve the formation and evolution of individual stars while being able to model the large-scale reionization. Recent state-of-the art examples include the CODA (Ocvirk et al. 2015), the CROC (Gnedin 2014) or the upcoming CODA-AMR (Aubert et al., in prep) simulations. All these projects aim at making predictions on populations of galaxies at $z > 6$ during the Reionization epoch and all this projects were massive high-performance computing challenges, with number of resolution elements in the $10^{10} - 10^{11}$ range. Such simulations are necessary to solve the tension that necessarily arises between the opposite requirements of a large simulated volume and a decent spatial resolution. All the aforementioned work used similar 64Mpc/h volumes with spatial resolutions in the $0.1 - 1$ kpc range: such spatial sampling is insufficient to model directly the in-situ impact of supernova feedback on galactic gas and rely on subgrid modeling. Likewise, it is evident that such simulations are unable to track the detailed structure of galaxies at these epoch.

On the other hand, the inclusion of such feedback is necessary as it impacts the gas properties (density, metallicity, kinematics) and stellar formation processes on spatial scales that are being resolved by these simulations. In addition, it has been found that population properties, such as the luminosity functions can be properly reproduced (Ocvirk et al. 2015; Gnedin 2014). Such studies cannot compete in terms of resolution with well-resolved studies of isolated objects (such as e.g. Wise & Cen (2009); Trebitsch et al. (2015); Rosdahl et al. (2016); Kimm et al. (2017)) but their goal is not to model the small scale physics at play but rather to be able to reproduce population and large-scale reionization properties. For the latter, the representativity of environments or the diversity of histories are expected to play a significant part (see e.g. Li et al. (2014)) : these aspects require large volumes and can't be described in zoomed simulations of isolated galaxies.

As a consequence, it is important to understand how the different types of feedback interact in such kind of large-scale and moderately resolved simulations. It's notably important considering objects close to the resolution limit ($10^8 - 10^9 M_\odot$ in our case) : such halos are numerous, possibly affected by photo-suppression ((Ocvirk et al. 2015)) and susceptible to outflows and large radiative escape fractions. Overall, their contribution to state-of-the art Reionization simulations must be understood and in particular the coupling between the different types of feedback. This work is presented in this perspective: using resolutions similar to the aforementioned large scale simulations, we aim at understanding how the global reionization properties and the galaxy populations produced by such models are shaped by the different feedbacks (radiative and supernova).

We introduce our models of star formation and feedback in Sec. 2. We then briefly describe the impact of the different feedback models on a single object in Sec. 3 and proceed to investigate how global star formation and reionization histories are influenced by the same models in Sec. 4. In Sec 5. we detail how the statistical

properties of halos are modified by the feedback with an emphasis on the hydrodynamical and radiative outflows at the virial radius. Conclusions and perspective are discussed in Sec. 6.

2 METHODOLOGY

In this section we describe our modeling of cosmic reionization with the EMMA code. We will take particular care to explain our supernova feedback implementation as well as our star formation prescription. We will finally give our initial set-up and the description of the different simulations studied in this paper.

2.1 Code description

We perform cosmological radiative hydrodynamic simulation with the EMMA (Aubert et al. 2015) code, an Adaptive Mesh Refinement (AMR) based code, designed to study the Epoch of Reionization (EoR). The code follows the evolution of three distinct physics: the colisionless Dark Matter (DM) dynamics, the gas dynamics, and the radiative transfer of ionizing photons with all the different modules self-consistently coupled to each other.

EMMA uses a fully threaded tree AMR description (Khokhlov 1998). The collisionless dynamics – dark matter and stars – use a particle based representation (Hockney & Eastwood 1981). The gravitational density field is determined from the particle using a Cloud In Cell (CIC) projection. The Poisson equation is solved using a multigrid relaxation method on the base level, and a Gauss-Seidel relaxation on the sub levels. The hydrodynamics solver is based on a piecewise linear method a la MUSCL-Hancock driven by HLLC Riemann solvers (Toro 1997). Finally, the radiation propagation is solved using a moment-based description, with the M1 closure approximation (Aubert & Teyssier 2008; Aubert & Teyssier 2010).

2.2 Star formation

In the two following subsections, we introduce our star formation and feedback models, as well as their free parameters. We are only focusing here on the general model implementation and all details about free parameters values used in this study can be found in Sec. 2.4.

To flag star forming regions, we use a simple over-density criterion δ . For every cells above this threshold, we compute the Star Formation Rate (SFR) :

$$\dot{\rho} = \epsilon_{SF} \frac{\rho_g}{t_{\rm ff}}, \qquad (1)$$

with ϵ_{SF} an efficiency parameter, ρ_g the local gas density and $t_{\rm ff}$ a local free fall time expressed as :
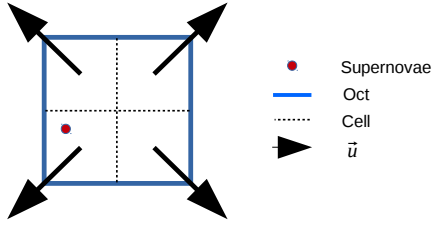
$$t_{\rm ff} = \sqrt{\frac{3\pi}{32 G \rho_g}}, \qquad (2)$$

This leads to the Schmidt law $\dot{\rho} \propto \rho_g^{1.5}$, close the deprojected observed Kennicutt relation (Kennicutt 1998).

Based on this SFR, we express the total mass to convert from gas to stars depending on the volume of the current cell dv and the current timestep dt:

$$M_\star = \dot{\rho} \cdot dv \cdot dt. \qquad (3)$$

We then follow Rasera & Teyssier (2006), and define a stellar

Figure 1. Kinetic energy injection scheme. No matter where the particle is in the oct, the explosion occurs radially from the center of the oct.

Name	ϵ_{SF}	f_{esc}	Supernovae	ϵ_{SN}
noFEED	0.5%	0	-	0
noSN/$\epsilon_{SN} = 0$	0.5%	0.4	-	0
$\epsilon_{SN} = 0.1$	0.5%	0.4	Kinetic	0.1
$\epsilon_{SN} = 0.5$	0.5%	0.4	Kinetic	0.5
$\epsilon_{SN} = 1$	0.5%	0.4	Kinetic	1
Thermal	0.5%	0.4	Thermal	1
Kinetic/SF05	0.5%	0.4	Kinetic	1
SF2	2%	0.4	Kinetic	1
SF10	10%	0.4	Kinetic	1

Table 1. Simulations features investigated in this study. The parameters are: the identification run name, the star formation efficiency ϵ_{SF}, photon escape fraction f_{esc}, type of supernovae feedback method and the efficiency of supernovae feedback ϵ_{SN}. All theses runs share the same initial conditions described in Sec. 2.4.

quantum mass of $m_\star$. Using $n_\star = \dfrac{M_\star}{m_\star}$, we compute an average number $n_\star$ of stellar particles to create. We finally draw the final number of particles $N_\star$ to inject in a Poisson law of parameter $n_\star$.

The star particles that are created are placed randomly in the cell volume with a velocity corresponding to the local gas velocity plus a component with a random direction and a random amplitude bound by the local sound speed.

2.3 Supernovae feedback

In this section, we discuss how we implement two different feedback methods. For both methods we dispose of a given amount of energy E_{SN} to inject in the hydrodynamical solver changing either internal or kinetic energy of the gas around the explosion.

2.3.1 Thermal feedback implementation

The thermal feedback model is the simplest way to inject energy and is used here mostly for comparisons. Such an implementation consists in the energy injection by modifying the local pressure:

$$\Delta P = \frac{E_{SN}}{dV}\,(\gamma - 1),\qquad(4)$$

where dV is the cell volume and the adiabatic index $\gamma = 5./3$.

Once the energy injection has been done, a fraction f_r of the stellar particle mass is returned and put back into the cell.

2.3.2 Kinetic feedback implementation

Historically, kinetic feedback was developed after it has been shown that thermal feedback suffers from high radiative losses and is inefficient to generate galactic outflows (Navarro & White 1993). Kinetic feedback consists into modifying the velocity of the gas in cells around the explosion instead of its internal energy. Its main advantage is that it warrants a greater conversion of heat into motion at our resolutions of interests.

But its main inconvenient its that it leads to a loss of resolution. Indeed, when a thermal scheme can heat an unique cell, the kinetic one needs to change the properties of the gas in a larger number of cells to result in a spherical explosion. Moreover, the larger the number of cells is, the more spherical the blast wave will be. On an AMR grid, finding neighbors has a cost and the counter part of a rounder explosion is that the numerical cost of finding the considered cells will quickly rise. Furthermore, due to the parallel nature of computations in EMMA , if an explosion occurs at an edge of a processor domain, distributing the explosion along the cells will result in costly communications. In our case, we limit the number of cells in which the explosion occurs to 8 and thanks to the AMR

oct-tree structure of EMMA , these eight cells share the same parent oct. This almost reduces to zero the cost of the neighbor search, and totally avoids communication between processors. Moreover, this also allows us to be sure that cells where the feedback is computed are all at the same level of resolution, which guarantees a certain homogeneity in the explosion. A schematic view of our injection scheme is given in Fig. 1.

We divide the total available energy, uniformly into these eight cells, so each cell receives,

$$e_{SN} = E_{SN}/8.\qquad(5)$$

Finally, e_{SN} is used to change the gas velocity of each cell,

$$\Delta\overrightarrow{v_{gas}} = \sqrt{\frac{2e_{SN}}{\rho_g.dV}}\,\overrightarrow{u},\qquad(6)$$

where $\overrightarrow{u}$ is the unit vector pointing radially from the center of the oct. The mass is returned in the same way as for the thermal feedback except that each cell now receives 1/8 of the total available mass.

2.4 Simulations parameters

Our stellar feedback model is intended to be used in large scale reionization simulation like CODA (Ocvirk et al. 2015). Such simulations are unique (e.g. $64 \cdot h^{-1}$ comoving megaparsecs (cMpc) cube , 4096^3 resolution elements for CODA) and cannot be used to test the stellar feedback parameters: for this purpose, we produce smaller boxes with equivalent resolutions. The goal of the set of simulations is to test our model and improve our understanding of the effects of stellar feedback parameters in large-scale cosmological simulations of the Reionization.

In the following, we consider a $(8 \cdot h^{-1}$ cMpc$)^3$ boxes $(\approx 12\text{cMpc})^3$, resolved with 256^3 dark matter particles. This leads to a DM mass resolution of $3.4 \cdot 10^6 \text{M}_\odot$, and a spatial resolution of 46ckpc on the coarse grid. The mass resolution is then one level below the resolution of the CODA simulation, but the spatial resolution is improved by the AMR of EMMA . Initial Condition (IC) were generated with MUSIC (Hahn & Abel 2011) with a Planck Cosmology (Planck Collaboration et al. (2015) : $\Omega_m = 0.3175$, $\Omega_v = 0.6825$, $\Omega_b = 0.0490$, $H_0 = 67.11$, $\sigma_8 = 0.830$. The simulations start at redshift $z = 150$ and share the same set of displacement phases. The grid is refined according to a semi-Lagrangian scheme, i.e. the cell

(a) Ionizing flux

(b) Cumulative mass return

(c) Cumulative energy return
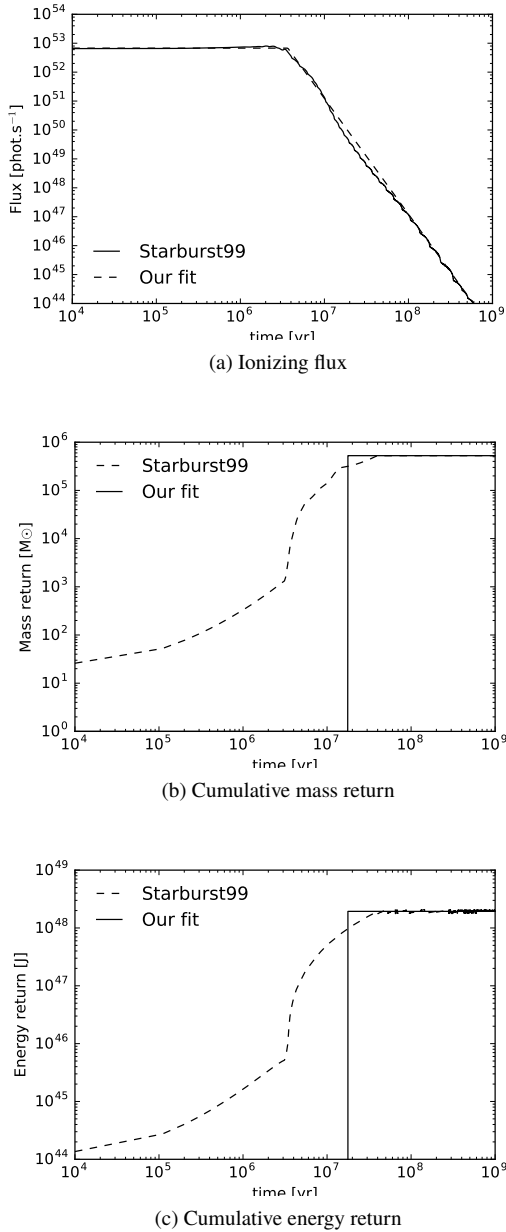
Figure 2. Our stellar model is calibrated with the Starburt99 model. The Starburst99 run considers a $10^6 M_\odot$ population with a Top Heavy IMF and a metalicity of Z=0.001. Our ionizing emissivity model (Fig. 2a) presents two phases, a constant emissivity one, and a decreasing one. The transition between theses two phases define the radiative lifetime $t_{\rm life}$. Mass (Fig. 2b) and energy (Fig. 2c) return from winds and supernovae are released instantaneously at the same time $t_{\rm SN}$.

is flagged for refinement if its dark matter or baryon mass exceed 8 times the equivalent mass of a coarse cell filled with the average dark matter or baryon density.The refinement is not allowed if the spatial resolution of the newly formed cells is under 500pc. In the goal to reduce the computational cost, we use a reduced speed of light of 10% of the real one, coupled with the Coarse Radiative Transport Approximation (CRTA) scheme implemented in the EMMA code (see Aubert et al. (2015)). This reduced speed of light decreases the cost of computation time by reducing the number of radiative time steps while still capturing properly the propagation of ionization fronts.

This value has been shown to provide results similar to the one obtained with the actual speed of light (e.g. Gnedin (2016) and also Deparis et al., in prep). The CRTA scheme propagates radiation at the coarse cell resolution (i.e. 46 comoving kpc in the current case) but photo-chemistry is performed at the finest resolution available (i.e. 500 pc in the current case). No additional UV background has been used.

We use a star formation over-density threshold of $\delta = 50$ and star formation efficiency parameter $\epsilon_{SF} = 0.5\%$. Our model for the ionizing emissivity of the star particles is calibrated using Starburst99 (Leitherer et al. 1999). Because our resolution does not allow to track real individual star particles, we consider that each star particle represents a stellar population of $7.2 \cdot 10^4 M_\odot$ with a Top-Heavy Initial Mass Function (IMF) (exponent 1.3 for $0.1 < m/M_\odot \leq 0.5$,2.3 for $0.5 < m/M_\odot \leq 1$ and 1.6 for $1 < m/M_\odot \leq 100$) integrated from $0.1 M_\odot$ to $100 M_\odot$ and with a constant metallicity of $Z = 0.001 = 0.05 Z_\odot$.

Since we are only considering hydrogen reionization, the Starburst99 spectrum is integrated on the energy range from 13.6eV to infinity. The ionizing emissivity presents two regimes (See Fig. 2a) with a constant phase followed by a fast emissivity drop. During the constant emissivity phase, sources emit $S_0 = 1.55.10^{17}$ phot.sec^{-1}.kg^{-1}. We consider the radiative lifetime $t_{\rm life}$ of sources to be at the transition of theses two regimes: $t_{\rm life} = 3.67 \times 10^6$Myr. After t_{life}, the sources still radiate with a number of photons that is a decreasing power law as a function of time ($S_{(t > t_{\rm life})} \propto t^{-4}$). The calculations are done using a single photon group with a mean energy of $< h\nu >= 23.42$ eV, an energy weighted cross section of $\sigma_e = 2.35.10^{-22}$ m^2 and a number weighted cross section of $\sigma_i = 1.82.10^{-22}$ m^2.

Supernova feedback model are also calibrated using Starburst99 as it gives us access to the temporal evolution of the amount of mass (Fig. 2b) and energy (Fig. 2c) returned in the medium by the considered stellar population. We choose to inject the totality of the available energy instantaneously after a time $t_{\rm SN}$ which is defined as the time where 50% of all the energy from Starburst99 should be released. We use the total amount of energy released by winds and supernovae during the whole lifetime of the population. The quantity of energy injected in our model is regulated by an efficiency parameter ϵ_{SN}. We return a mass fraction f_r of the total particle mass when a supernova explodes. All the mass is released instantaneously at the same instant as the energy. In practice, our model parameters are: an injection time of $t_{\rm SN} = 17.7$ Myr, a total available energy of $E_{SN} = 2.47 \cdot 10^{42}$J.M$_\odot^{-1}$ and a mass return fraction of $f_r = 52.6\%$.

Tab. 1 presents a summary of the different runs performed in this study. It should be noted that we did not attempt to calibrate the simulations to satisfy observational constraints (here the star formation rate and ionization fraction history). The latter are given to indicate that the runs deliver reasonable results but given the small simulated volumes or the limited range of halo masses (the most massive halo has $M \approx 10^{11} M_\odot$), our simulations may lack the statistical representativity of objects, scales or environments. Enforcing an exact reproduction of observational constraints would be of limited scope and we focus rather on differential comparisons between runs using different physics.
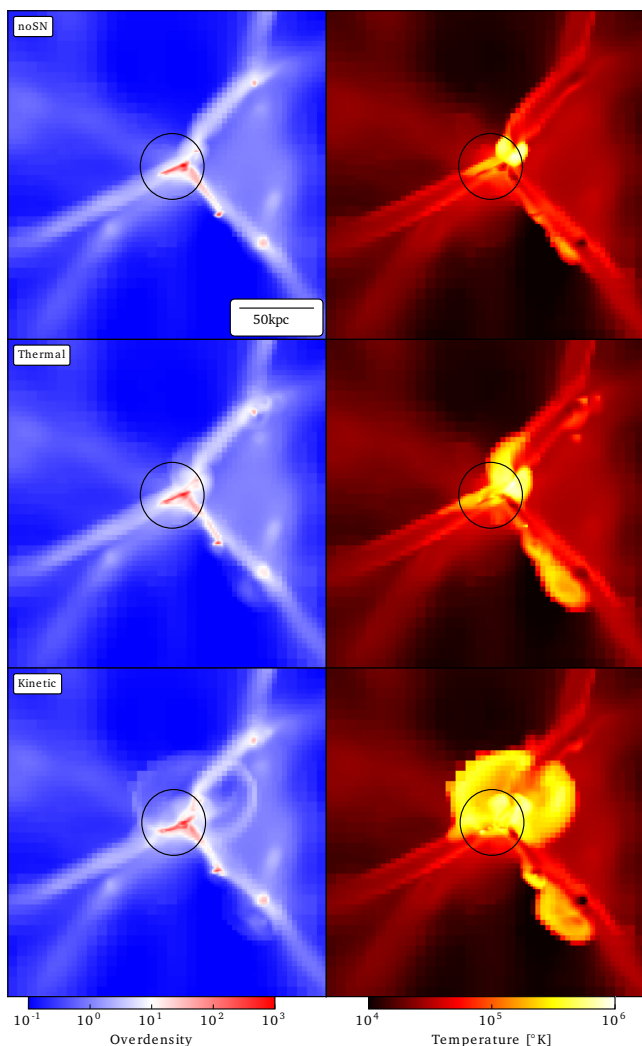
Figure 3. Most massive halo of the simulation (M≈ 10^{11}M$_\odot$) at redshift $z = 6$. Average over a 7kpc thick slice of overdensity (left) and temperature (right), without feedback (top), with thermal feedback (middle) and with kinetic feedback (bottom). The black circle represent the R_{200} = 21kpc. With the same quantity of energy injected, kinetic feedback can generate much bigger hot bubble ($T > 10^5 K$) around halo than thermal one.

3 TEMPERATURE AND DENSITY FIELDS AROUND THE MOST MASSIVE HALO

Our first diagnostic is purely qualitative and consists in looking at the density and temperature fields around a specific halo. We choose the most massive halo in the *noSN* simulation, which has a mass of M= $1.10 \cdot 10^{11}$M$_\odot$, corresponding to a R_{200} radius of 21kpc at redshift $z = 6$. Fig. 3 represents a 214×214×6.5 kpc slice at redshift $z = 6$, centered on this halo, for simulation without supernovae feedback (first row), with direct thermal injection (middle row) and with our kinetic model (bottom row).

The density map of the *thermal* run is a bit more fluffy around the main over-densities (in red) than the one of the *noSN* run. A thin concentric over-dense region (in white) appears around some halos, for example in the top right filament or around the further over-density in the bottom right filament. These shells are due to the shock of the outflowing gas on the IGM. The main halo is able to generate a bigger hot bubble (yellow region in temperature maps) in the *thermal* run than in the *noSN* run. Differences are also clear

on the bottom right filament where a hot bubble was almost absent in the run without feedback.

If we now look at the *kinetic* run, we clearly see a more important impact on both fields than with the thermal injection method. Outflows are significantly stronger and shock shells appear around the main halo with a radius of several R_{200} and a density of about ten times the average density (in white). Furthermore, the hot region is also wider and corresponds to the inner shock radius defined by the shells in the density map.

The hot region ($T > 10^5$K) in a $5 \times R_{200}$ box around the halo represents a volume fraction of $f_V = 0.3\%$ and a total mass of $M_{hot} = 1.9 \cdot 10^9 M_\odot$ for the *noSN* run, compared to $f_V = 1.0\%$ and $M_{hot} = 4.2 \cdot 10^9 M_\odot$ for the thermal run and $f_V = 2.7\%$ and $M_{hot} = 7.3 \cdot 10^9 M_\odot$ for the kinetic run. Around this specific halo, the kinetic feedback can heat 2.7 times more volume and 1.7 time more mass of gas. Despite our limited resolution and our reliance on subgrid models to introduce stellar feedback, it is clear that it has an impact on scales that are in turn resolved in our simulations: its impact on predictions of the large-scale Reionization should therefore be investigated further.

4 STAR FORMATION AND IONIZATION HISTORIES

We investigate the cosmic star formation rate and ionization fraction history. We expect a direct link between ionization history and the SFH as ionizing photons are mainly emitted by newly formed stars (see our ionizing emissivity model on Fig. 2a) but we will see that this link is not as direct as expected at the resolution of interests.

In this section we look at how a change in the energy injection model, in the star formation efficiency or in the amount of energy injected influence theses two observables.

4.1 Influence of radiative and supernovae feedback

We want to explore the influence of the energy injection method on the regulation of star formation, so we compare three simulations, one without feedback, one with thermal feedback , and one with kinetic feedback. These three simulations are run with radiative transfer and with the same initial setup. In addition to these three simulations, we use a reference simulation without radiative sources to measure the influence of radiative transfer feedback.

We observe on Fig 4a that the injection method significantly changes the cosmic SFH. The *Thermal* run (in red) produces a SFR slightly lower than the *noSN* run (in black), and as expected is not as efficient as the kinetic model to regulate star formation. With the same amount of injected energy by unit mass of formed stars, at redshift $z = 6$ the SFR of the *Kinetic* run (in green) is lowered by a factor ≈ 3, compared to the *noSN* run (in black). Star formation processes are dependent of the gas density, which is itself strongly dependent on the resolution. The bump in the SFH at redshift $z \approx 10$ is due to the creation of the last refinement level $L_{max} = 11$ at redshift $z = 10.6$.

For each methods, the feedback decreases the SFR, so the total number of emitted photons is not the same between simulations. But we observe on Fig. 4b that the end of the Reionization occurs almost at the same redshift in these 3 simulations. The small delay between their reionization redshift is in accordance with their SFH, ie a lower SFH leads to a later reionization. But this delay is smaller than what we could expect just from the lowering of the photon budget. Indeed, at redshift $z = 8$, the kinetic feedback decreases the SFR by a factor ≈ 3 and thus the number of emitted photon
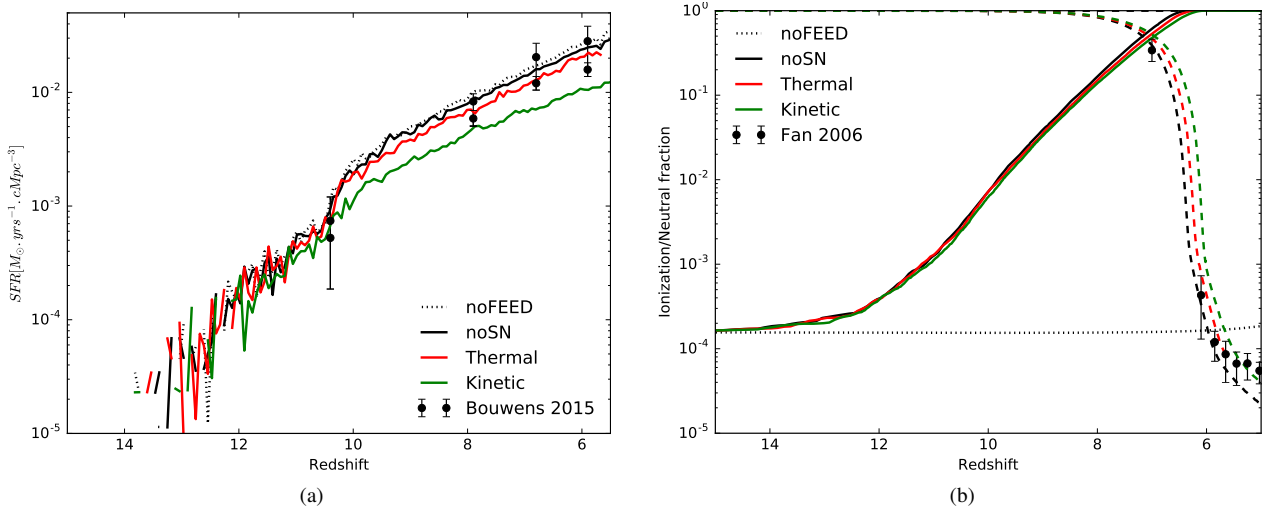
Figure 4. (a) Cosmic star formation histories and (b) volume weighted ionization (solid lines) and neutral (dashed lines) fraction function of redshift for different feedback method. The introduction of radiation get a small impact on the cosmic SFH. The kinetic method get a significantly stronger effect on the SFH than the thermal model. Reionization occurs almost at the same redshift independently of feedback scheme.

is also lowered by approximately the same factor : meanwhile, the ionization rate (given by the slope of the ionization history curve) is surprisingly unaffected. This point is investigated further in section 5.4.

If we only focus on radiative feedback effects, by comparing the differences between the *noFEED* run and the *noSN* run, we can quantify the influence of radiation on the SFH. On Fig. 4a we observe that the *noFEED* run (in black dot) yields almost the same SFH than the *noSN* run (in black). Obviously, the *noFEED* run (black dotted curve on Fig. 4b) does not reionize and stays with an ionization fraction only governed by collisional ionizations. The fact that radiative feedback does not regulate cosmic star formation history implies that it does not influence halos responsible of the global SFH. We will see in section 5 that radiation has an impact on low mass haloes, which are responsible only for a small part of the global SFH.

4.2 Influence of the supernovae feedback efficiency parameter

The supernovae feedback efficiency parameter ϵ_{SN} regroups all the subgrid physics that we do not resolve, like radiative energy losses on small scales, reducing the overall energy budget available to the feedback. In practice, it can also act as a free parameter to mimic the impact of IMF, by changing the fraction of stellar mass available to explosions. Here we only explore efficiencies lower than unity, but one could imagine higher ones to mimic unresolved effect that prevent the gravitational collapse, such as turbulence.

We run four simulations with different feedback efficiencies ($\epsilon_{SN} = 0$; $\epsilon_{SN} = 10\%$; $\epsilon_{SN} = 50\%$ and $\epsilon_{SN} = 100\%$), and look at how cosmic star formation and ionization histories are impacted by a change in the amount of energy injected. Resulting star formation and ionization histories are presented on Fig. 5. As expected, the more energy we inject, the more we reduce the global SFR (Fig. 5a). Furthermore, we observe the same behavior as the previous section: the regulation of star formation by supernovae feedback does not significantly change the reionization history (Fig. 5b).

We note that the run with the $\epsilon_{SN} = 0.1$ efficiency shows a

comparable SFH to the one of the *Thermal* run with 100% efficiency (red curves in both Fig. 4a and Fig. 5a): at our resolution and in this context, the thermal feedback scheme presents a 90% of losses compared to the kinetic scheme.

### 4.3 Influence of the star formation efficiency parameter

We now explore the link between the star formation efficiency parameter ϵ_{SF} and the supernovae feedback. Indeed, increasing star formation efficiency leads to transforming more gas into stars, and thus increasing the amount of feedback, but increasing the feedback results in decreasing the star formation rate. It is not clear how the simulation will respond to a change in the star formation efficiency with a given supernovae feedback.

We use the kinetic feedback scheme with an efficiency of $\epsilon_{SN} = 100\%$ and run three simulations with star formation efficiency of $\epsilon_{SF} = 0.5\%$, $\epsilon_{SF} = 2\%$ and $\epsilon_{SF} = 10\%$.

Fig. 6a presents the obtained star formation histories: increasing star formation efficiency leads to first stars at higher redshift and in greater quantity. Later on, the feedback becomes sufficiently strong to change the shape of the SFH.

At high redshift, the SFH seems to be simply regulated by the ϵ_{SF} parameters: the larger ϵ_{SF} is, the more stars are being formed. At later times, the amount of injected energy with high star formation efficiency ($\epsilon_{SF} = 10\%$, in blue) becomes sufficient to generate a decreasing star formation history. As increasing feedback does not just shift the whole SFH at lower values but significantly change its shape, we conclude that we cannot fit any arbitrary large SFH, even by increasing the star formation efficiency. It should be noted that the actual efficiency turning-point value is likely to depend on the simulations properties such as the box size and the abundance of massive objects but similar effects were already observed in (Gillet et al., in prep with RAMSES-CUDATON) at similar resolutions.

If we now pay attention to the ionization histories (Fig. 6b), we observe a significant change in the reionization redshift. As expected, the more efficient the star formation is, the sooner the end of reionization happens. As stars appear sooner in the volume with higher star formation efficiency, the medium starts to reionize
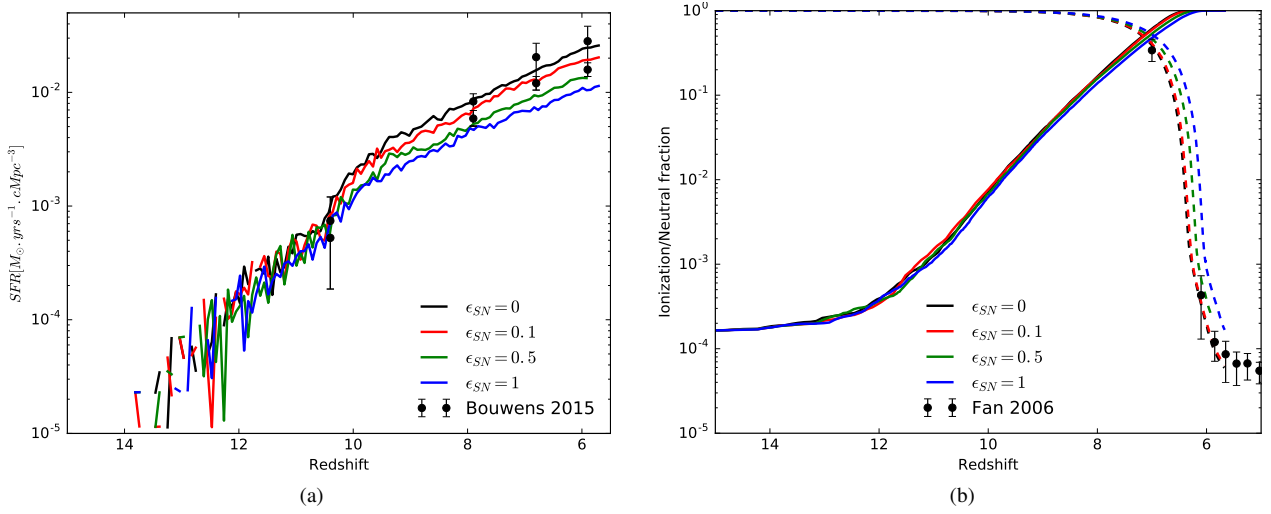
Figure 5. (a) Cosmic SFH and (b) volume weighted ionization (solid line) and neutral (dashed line) fraction function of feedback efficiency parameter ϵ_{SN} for the kinetic feedback model. The regulation of star formation is directly linked with the quantity of energy injected in the medium. The ionization history is not impacted by the change in the SFH due to supernovae feedback.
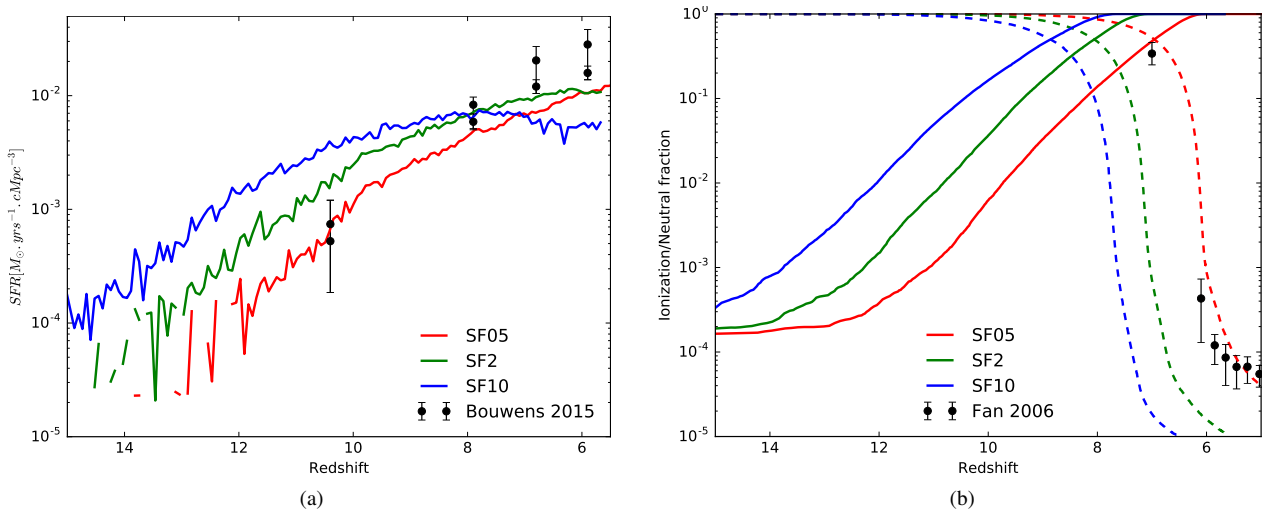
Figure 6. (a) Star formation and (b) volume weighted ionization histories for different star formation efficiencies ϵ_{SF} with high efficiency ($\epsilon_{SN} = 1$) kinetic feedback. Due to feedback, increasing star formation efficiency can lead to lower the SFR.

at higher redshift. But as the feedback needs time to be efficient at regulating the SFR, it also needs time to regulate the ionization rate.

There is a small change in the slope of the *SF10* ionization curve (in blue on Fig. 6b) after redshift $z \approx 11$, due to the decrease of the SFR. But the effect of feedback does not seem to be sufficient to stop the reionizing processes, at least in the range of parameters we explore. However, it may be possible that the SFR cutout will be sufficient to prevent the box from reionizing if we push the efficiency further.

5 HALO-CENTRIC STUDIES

5.1 Halos mass function

We now focus on the properties of the halo population. Halos are detected using the Friends-Of-Friends algorithm of PFOF (Roy et al.

2014) providing ~ 18000 objects with a least 10 particles and ~ 200 with at least 1000 particles ($M \sim 3 \times 10^9 M_\odot$).

Stars are associated to a halo if they are within its R_{200}. The R_{200} defined as the radius where the average density of the halo correspond to 200 times the average dark matter density:

$$R_{200} = \left(\frac{3 \cdot M_{fof}}{4\pi \cdot 200 \bar{\rho}} \right)^{1/3}, \qquad (7)$$

with $\bar{\rho} = (\Omega_m - \Omega_b) \frac{3H_0^2}{8\pi G}$ the average dark matter density in the universe and M_{fof} the halo mass given by PFOF. The z=6 halos mass functions (HMF) are presented on Fig. 7. We observe no measurable impact on the HMF function of the feedback type. The mass function is typical of AMR code: it is complete for masses $> 10^9 M_\odot$ corresponding to ~ 300 particles and presents a factor 2 deficit for $M \sim 3 \times 10^8$ (100 particles). At the high mass end,
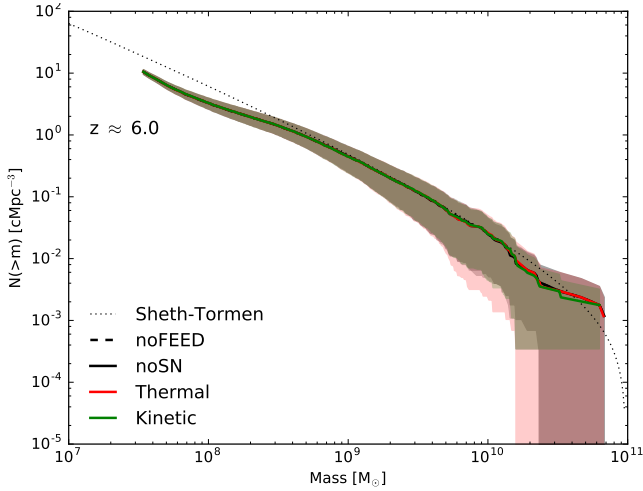
Figure 7. Cumulative halos mass function (HMF) for different feedback types and 100% efficiency at redshift z=6.

some deficit in the number of massive halo can be seen from masses $> 1.5 \times 10^{10} M_\odot$, due to the limited box size.

5.2 Star formation

The balance between star formation and feedback, functions of halo mass, is not trivial. Indeed, low masses halos ($M < 10^9 M_\odot$) do not form much stars and thus are not exposed to a large amount of feedback. However if a stellar population forms in these light halos, supernovae events can expel a significant part of the gas. On the other side, high mass halos ($M > 10^{10} M_\odot$) host large star formation events and are exposed to strong feedback processes, but their gravitational potential is much more able to keep their baryons trapped. Moreover low-mass halos ($M < 10^9 M_\odot$) are predominant in number but they exhibit a lower SFR, so they do not host large quantity of UV emitting stars. Conversely, high-mass halos do emit a strong UV field but are far less numerous. What are the respective contributions of each classes of masses on the photon budget and how is this budget influenced by feedback?

We compute instantaneous star formation rate for each halo by measuring the total stellar mass created within its R_{200} during the last 10Myr :

$$SFR_{10}^{halo} = \frac{\sum M_\star \left(r < R_{200}^{halo}; t < 10\text{Myr} \right)}{10\text{Myr}}. \tag{8}$$

The correlation between the halo mass and its instantaneous SFR is presented on Fig. 8a. In all cases, the introduction of feedback leads to decreasing the SFR and changes the slope of this correlation. Radiative (in plain black) and thermal feedback (in red) tend to be more efficient at lowering the SFR for low masses halos ($M < 10^9 M_\odot$) while kinetic feedback (in green) tends to act on heavy halos ($M > 10^{10} M_\odot$).

If we now look at SFR_{bin}, the total contribution of a class of halos masses to the cosmic SFR:

$$SFR_{bin} = \sum_{halo} SFR_{10}^{halo} \left(M_{bin} \leq M^{halo} < M_{bin} + dM \right), \tag{9}$$

presented on Fig. 8b, we see that smallest halos ($M < 3 \times 10^9 M_\odot$) do not dominate the global SFR at this time, even if they are the most numerous. Meanwhile, halos with masses $> 10^{10} M_\odot$ are the


(a)

(b)
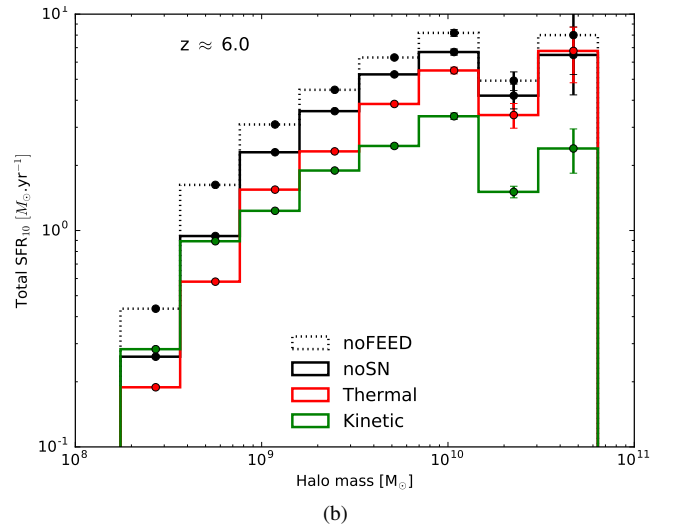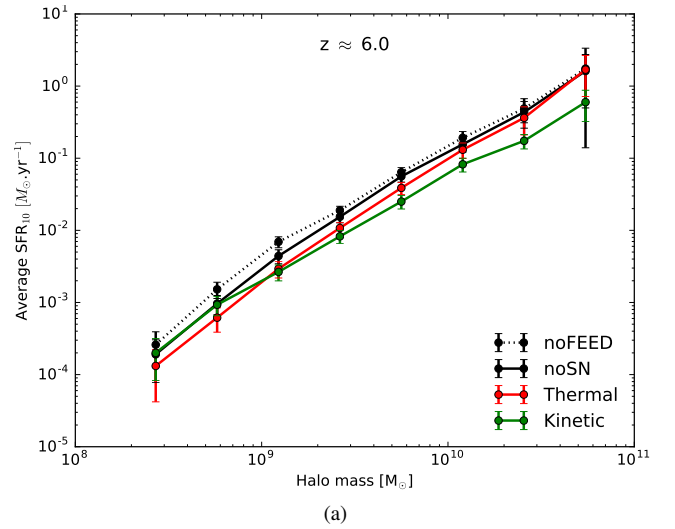
Figure 8. Star formation rate averaged (a) and binned (b) by bins of halo mass at redshift z=6 for different feedback methods.

main contributors of the cosmic SFR at $z = 6$. To alter the cosmic SFH, a feedback scheme has to change SFR in the predominant class of halos masses. We see from Fig 8a that kinetic injection is the most efficient to regulate star formation in this range of masses ($M > 10^{10} M_\odot$), and thus the most efficient to regulate the global SFR. As a corollary, it shows that halos under $3 \times 10^9 M_\odot$ are not the main contributors of the UV photon production (which is dominated by newly formed stars). This production is dominated by more massive objects which are the most sensitive to the feedback : as seen previously, this sensitivity however do not translate into a significant modification of the reionization history.

5.3 Average R_{200} flow speed

In this section, we investigate the evolution of the average radial velocity of the gas around halos depending on the feedback scheme. To compute these velocities, we draw a virtual sphere around each halo with a given radius and centered on the center of mass of the halo. The resulting velocities are a function of the distance from the halo. Here we arbitrary take R_{200} as our reference radius.
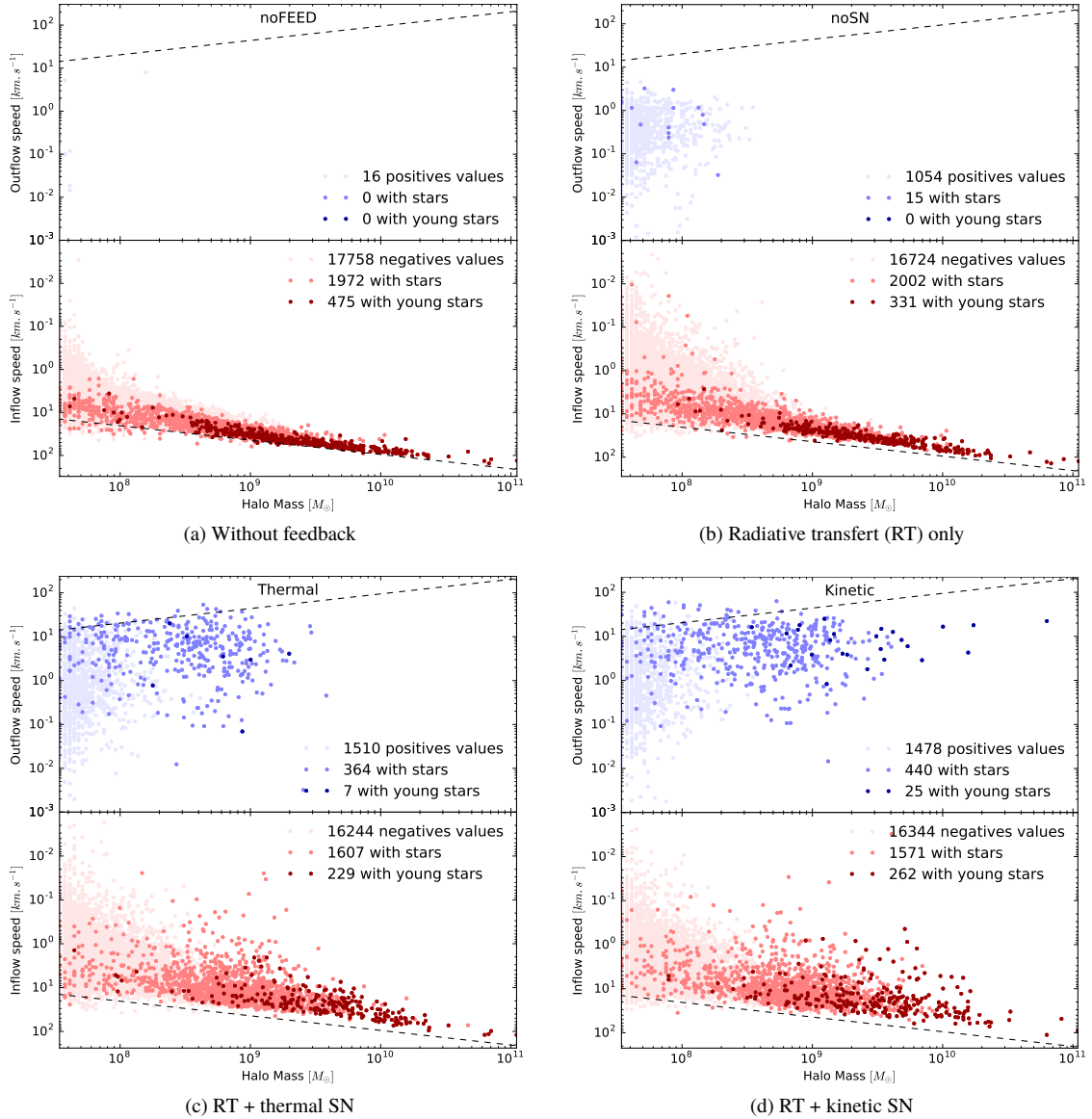
Figure 9. Average radial hydrodynamical flow speed at R_{200} function of injection method measured at redshift z=6. Blue dots represent halos with outflow, red with inflow. Light dots represent halos without stars while dark dots stand for halos with stars. The dashed line represents $\pm$ the escape velocity. Without radiation there is almost no halo with a positive average speed (outflowing matter). The introduction of radiation leads to the apparition of a population of starless low mass halos ($M < 3 \cdot 10^8 M_\odot$) with outflow. Supernovae introduce a population of outflowing halos with stars. Kinetic feedback allows heavier halos to get outflow than thermal feedback.

The general expression for the average radial velocity $\bar{v}$, is:

$$\bar{v} = \frac{\oint \vec{v} \cdot d\vec{s}}{\oint d\vec{s}}, \qquad (10)$$

with $d\vec{s}$ the surface element of the R_{200} sphere. Each sphere is discretized with 3072 HEALPix elements of equal area (Górski et al. 2005), the average radial velocity becomes:

$$\bar{v} = \frac{1}{N} \sum_{i=1}^{N} \vec{v_i} \cdot \vec{r_i}, \qquad (11)$$

with N the number of HEALPix points, $\vec{v_i}$ the gas velocity of the nearest cell of point i and the normal vector $\vec{r_i}$ oriented outward.

Therefore, positive values stand for outflow and negatives one for inflow. Fig. 9 presents the resulting average velocities as a function of halo masses for the different feedback schemes. Each halo is represented by a dot, with a different color indicating if it has stars, young stars ($t_* < t_{life}$) or no star. The upper part of the diagram represents outflows and the lower part represents inflows.

The dashed lines are defined by:

$$v_{lim} = \pm \sqrt{\frac{2GM_{(r<R_{200})}}{R_{200}}}, \qquad (12)$$

and represent the free fall velocity limit for the inflowing case, and the escape velocity for the out-flowing case.

Without feedback (Fig. 9a) almost all halos are in the negative

part of the diagram, they are all accumulating baryons. The correlation between inflow speeds and halo masses is particularly sharp with this run, and at this redshift ($z = 6$).

This free fall tendency tends to be an upper limit of the accretion velocity, and only few halos have average inflow velocity with an absolute value over this limit. Also, we note that the velocity dispersion becomes wider as halos becomes less massive.

With the introduction of radiation (Fig. 9b), there is an increase in the dispersion of velocity values. This increase is more pronounced on halos lighter than $3 \cdot 10^8 M_\odot$ and specially starless ones (light red population) at a point that a part of this population starts to get net outflows (in light blue). The fact that the major part of this population does not have stars, indicates that theses outflows are not due to internal feedback, and suggest an external effect. Our interpretation is that these light halos are submitted to a UV field created by surrounding halos massive enough to get a significant amount of young stars. We are observing the effect of photo-heating by radiative feedback, the gas heated by radiation expands and leaves its host by dilution. Meanwhile, heavier halos can hold their baryons thanks to their deeper potential.

With an average speed of $\approx 0.5 \text{km.s}^{-1}$ theses outflows are relatively slow and all velocities are below the escape velocity, so baryon are still bounded to their host.

We show in Sec. 4.1 that radiation has a negligible impact on the cosmic SFR, but we observe here that it can generate outflows for low mass halos. These two points are not in contradiction, as we show in Sec. 5.2 that these low mass halos represent a small part of the global SFR in our simulations. So radiation does have an impact on star formation but only on halos with a small contribution to the global star formation.

There is also a small shift, present for almost all the halos mass range, in inflowing speeds: inflows tend to be slightly slower due to photo-heating. Radiation generates outflows and slows down the collapse of gas, reducing the quantity of available star forming material by limiting the accretion.

If we now focus on the two runs with supernovae feedback (Fig. 9c and 9d), we clearly see that there is a new population of halos with outflows and that almost all those halos have stars (dark blue). Supernovae feedback also limits the accretion, the dispersion of inflowing halos with stars (dark red) is significantly increased. This idea is supported by the fact that the distribution of starless halos stay mainly unchanged compared to RT only run (Fig. 9b).

The mean outflow speed is now close to 10km.s^{-1} which is twenty times greater than for the *noSN* run. Some light halos ($M < 10^9 M_\odot$) present an average outflow speed greater than the escape velocity: the feedback is able to disperse material out of these objects. It seems that the feedback type does not change the maximum outflow speed ($\approx 60 \text{km.s}^{-1}$), while only large halos present a positive average speed. The most massive halo with outflow in the *noSN* simulation weight $3.5 \cdot 10^8 M_\odot$, $3.6 \cdot 10^9 M_\odot$ in the *thermal* run and $6.3 \cdot 10^{10} M_\odot$ in the *kinetic* run. Outflow velocities can seem low compared to observed ones (between ≈ 20 and $\approx 2000 \text{Km.s}^{-1}$ according to Veilleux et al. (2005)) but we are considering averaged values: locally on the virial spheres, velocities can be as high as 600km.s^{-1} at the R_{200} level, and 1500km.s^{-1} in a cell where the explosion occurs, which is in the typical range of observed velocities.

5.4 Influence of supernovae feedback scheme on R_{200} halo emissivity

Due to the moment based treatment of radiation, we can use a procedure similar to our hydrodynamical analysis (Sec 5.3) to compute F_{200}, the halo emissivity at R_{200}, by integrating the radiative flux field $\vec{F}_{rad}$ for each halo:

$$F_{200}^{halo} = \oint_{R_{200}^{halo}} \vec{F}_{rad} \cdot d\vec{s}. \tag{13}$$

Also, in a similar way that in Eq. 9, we can sum these F_{200} by mass bins, and estimate the photon budget distribution:

$$F_{bin} = \sum_{halo} F_{200}^{halo} \left(M_{bin} \leq M^{halo} < M_{bin} + dM \right). \tag{14}$$

These quantities measure the photons that escapes from halos into the IGM, i.e. the effective contribution of halos or classes of masses to the cosmic reionization. Fig. 10a presents F_{bin}, the total emissivity of halos in a range of masses for our three feedback schemes.

First, it appears that there are two regimes in this diagram: most massive halos represent the biggest part of the emissivity while lightest ones contribute about ten times less. Also, it seems that the total emissivity of heavier halos tends to decrease with the halo mass, however it is not clear if it is a physical effect or a statistical effect due to the box size we are considering ($\approx 12 \text{ cMpc}$)^3 and the low abundance of such massive haloes. We have to take into consideration that we are using the Coarse Radiative Transport Approximation (CRTA), ie the radiative transport computations are only executed on the coarsest grid. At the scale of a coarsest cell, the radiation field can be considered as a homogeneous UV background. The dashed line represents $M_{min} = 3.3 \cdot 10^9 M_\odot$, the mass of a halo with R_{200} equals to the radiative transport resolution limit. As such, fluxes vary slowly as a function of radius and F_{200} tends to scale with the halo size.

Nevertheless, halos with masses over M_{min} are responsible of the major part of the photon budget of our simulations. Approximately 80 % of photons are coming from these halos :

$$\frac{\sum \dot{N}(M > M_{min})}{\sum \dot{N}} \approx 80\%, \tag{15}$$

with $\dot{N}$ the stellar particle emissivity belonging to the current halo, and for those ones, the feedback scheme does almost not change the total emissivity at the R_{200} level (Fig. 10a). We noted in Sec. 4.1 and more particularly on Fig. 4, that the feedback scheme did not change reionization history : this is because feedback does not change the halo F_{200} emissivity.

Moreover the order of these curves is in accordance with the order found in Fig. 4b: the F_{200} halo emissivity of the kinetic run is slightly lower than the two other runs, and so its reionization happens last.

If we finally compute the ratio of these F_{200} halo emissivities to $\dot{N}$ their internal radiative sources (directly linked to the integrated SFR presented in Fig. 8b), we obtain a rough estimation of f_{esc}, the photon escape fraction. The escape fraction is computed using prescription of (Kimm et al. 2017), ie we consider the time needed by photons to travel from the halo center to R_{200}:

$$f_{esc} = \frac{F_{200}}{\sum \dot{N}_{\left(t - \frac{R_{200}}{\bar{c}}\right)}}. \tag{16}$$

Fig. 10b presents this averaged escape fraction as a function of halo masses.

(a) Total R200 emissivity

(b) Estimated average escape fraction
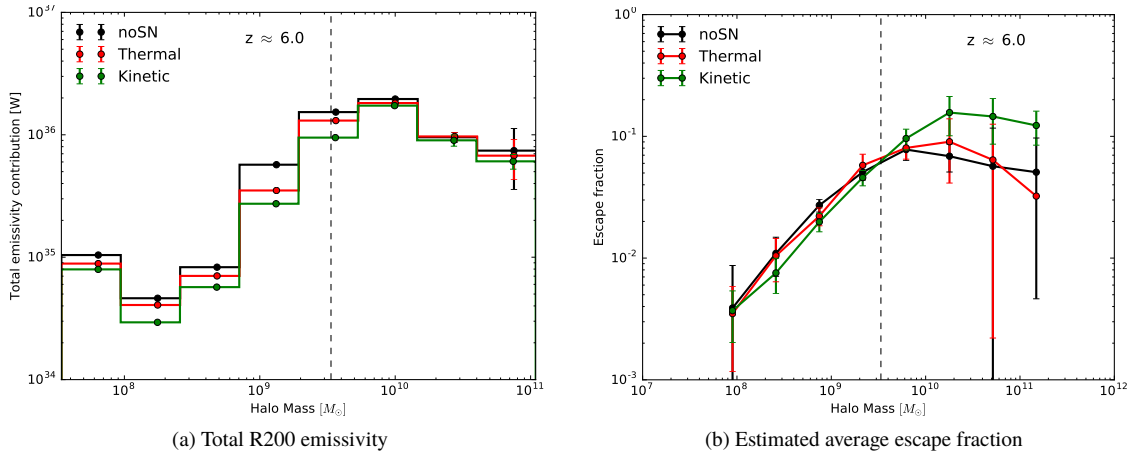
Figure 10. Total R_{200} emissivity contribution (a) and escape fraction (b) as a function of halo mass, for different feedback scheme. All measures are done at redshift z=6. The dashed line represents the halo mass equivalent to our radiative resolution limit. For massive ($M > 10^{10} M_\odot$), radiatively well resolved halos, emissivity stays almost identical independently of the feedback scheme. We observe a significant increase in the escape fraction of massive halos with the kinetic scheme.

For halos under M_{min}, the observed linearity of the relation is due the limited resolution. For greater masses, we observe an increase of the escape fraction for heaviest halos ($M > 10^{10} M_\odot$) for the kinetic feedback scheme. This explains how the run with kinetic feedback reionize as quickly as other runs, despite its lower SFR: massive halos form less stars but they are more efficient at releasing their photons into the IGM.

The increase of photon escape fraction by supernovae feedback we measure confirm previous works such as eg Kimm & Cen (2014) or Trebitsch et al. (2015).

6 CONCLUSION AND DISCUSSION

We discuss the impact of supernova and radiative feedbacks on simulations of the Reionization process. The level of approximation and resolution envisioned here is the one used in large scale simulations of the process : in-situ physics of the impact of feedback within galaxies cannot be fully captured but the focus is put on the diversity of situations with halo populations where e.g. environmental effects are included such as the photo-suppression of star formation by external radiation.

For this purpose, we present a simple scheme of supernovae energy injection in AMR cosmological simulation of reionization. We test this model by running a set of fully coupled radiative hydro-dynamic simulations with kiloparsec resolution, similar to CODA (Ocvirk et al. 2015), varying feedback implementation and model free parameters. We show that this feedback scheme is able to regulate star formation and generate galactic winds on a wide range of halo masses. We took the opportunity of this set of simulation to assess the interplay between the different kind of feedbacks at resolutions relevant to CODA-like runs. Here are our main observations:

• Even with a strong regulation of the SFR, and thus of the number of emitted photons, this increase of the escape fraction leads to a comparable number of photons reaching the IGM and thus a similar reionization history. The expulsion of baryons by feedback creates escape paths for the radiation.

• The escape fraction of photons of halos with masses over $10^{10} M_\odot$ is increased by a factor ≈ 3 by our kinetic feedback scheme.

• As a consequence, we find that the photon budget is mainly governed by massive halos ($M > 10^9 M_\odot$) (Fig. 10a).

• Runs with radiation produce a population of low mass ($M < 10^9 M_\odot$) halos with outflowing gas (Fig. 9b). We interpret this population as being photo-heated, losing their baryons by photo-evaporation.

Simulations with larger volume will be used to improve statistics in the range of mass$10^{10} M_\odot < M < 10^{11} M_\odot$ and explore if the decrease in photon budget for halos more massive than $10^{10} M_\odot$ observed in Fig 10a continues to higher masses. Meanwhile, the small simulations studied here are often used for calibrations of reionization histories of larger productions. Our results have some impact on this aspect, with two opposite possibilities:

• our boxsize captured the most productive range of halo masses and the contribution to the escaping photon budget of halos with $M > 10^{10} M_\odot$ decreases. Such kind of simulations can be valuable outside of pure comparative purpose for calibration of larger runs.

• our small boxes do not capture all the effective sources of reionization and the escaping photon budget could be dominated by halos beyond our most massive objects. Hopefully, there exists a larger simulation scale where a high mass cutoff in the effective photons contribution appears. However current grand challenge simulations (CROC, CODA) are not much bigger (8 Mpc Vs 64 Mpc) than the one used here, with similar resolution : if test simulations larger than the one presented here are required, the relative cost of calibration to production could become problematic.

Preliminary CODA analyses tend to be in favour of the first scenario, and it seems that $64 c Mpc^3$ boxes also present a maximum in the photon budget around a halo mass of $10^{10} M_\odot$ (Lewis et al., in prep.).

REFERENCES

Aubert D., Teyssier R., 2008, Monthly Notices of the Royal Astronomical Society, 387, 295

Aubert D., Teyssier R., 2010, ApJ, 724, 244

Aubert D., Deparis N., Ocvirk P., 2015, Monthly Notices of the Royal Astronomical Society, 454, 1012

Bouwens R. J., Illingworth G. D., Oesch P. A., Caruana J., Holwerda B., Smit R., Wilkins S., 2015, The Astrophysical Journal, 811, 140

Chardin J., Puchwein E., Haehnelt M. G., 2017, Monthly Notices of the Royal Astronomical Society, 465, 3429

D'Aloisio A., Upton Sanderbeck P. R., McQuinn M., Trac H., Shapiro P. R., 2016, preprint, 1607, arXiv:1607.06467

Dubois Y., Teyssier R., 2008, Astronomy and Astrophysics, 477, 79

Giallongo E., et al., 2015, Astronomy and Astrophysics, 578, A83

Gnedin N. Y., 2014, arXiv:1403.4245 [astro-ph]

Gnedin N. Y., 2016, ApJ, 833, 66

Górski K. M., Hivon E., Banday A. J., Wandelt B. D., Hansen F. K., Reinecke M., Bartelmann M., 2005, ApJ, 622, 759

Haardt F., Madau P., 2012, The Astrophysical Journal, 746, 125

Hahn O., Abel T., 2011, Monthly Notices of the Royal Astronomical Society, 415, 2101

Hockney R. W., Eastwood J. W., 1981, Computer Simulation Using Particles

Iliev I. T., Mellema G., Ahn K., Shapiro P. R., Mao Y., Pen U.-L., 2014, Monthly Notices of the Royal Astronomical Society, 439, 725

Katz N., 1992, The Astrophysical Journal, 391, 502

Kennicutt J., 1998, The Astrophysical Journal, 498, 541

Khokhlov A., 1998, Journal of Computational Physics, 143, 519

Kimm T., Cen R., 2014, The Astrophysical Journal, 788, 121

Kimm T., Cen R., Devriendt J., Dubois Y., Slyz A., 2015, arXiv:1501.05655 [astro-ph]

Kimm T., Katz H., Haehnelt M., Rosdahl J., Devriendt J., Slyz A., 2017, Monthly Notices of the Royal Astronomical Society

Leitherer C., et al., 1999, The Astrophysical Journal Supplement Series, 123, 3

Li T. Y., Alvarez M. A., Wechsler R. H., Abel T., 2014, ApJ, 785, 134

Navarro J. F., White S. D. M., 1993, Monthly Notices of the Royal Astronomical Society, 265, 271

Ocvirk P., et al., 2015, preprint, 1511, 11

Planck Collaboration et al., 2015, preprint, 1502, arXiv:1502.01589

Rasera Y., Teyssier R., 2006, Astronomy and Astrophysics, 445, 1

Rosdahl J., Schaye J., Dubois Y., Kimm T., Teyssier R., 2016, preprint, 1609, arXiv:1609.01296

Roy F., Bouillot V. R., Rasera Y., 2014, Astronomy and Astrophysics, 564, A13

Stinson G., Seth A., Katz N., Wadsley J., Governato F., Quinn T., 2006, Monthly Notices of the Royal Astronomical Society, 373, 1074

Toro E. F., 1997, Riemann solvers and numerical methods for fluid dynamics : a practical introduction. Springer, Berlin, New York, http://opac.inria.fr/record=b1093563

Trebitsch M., Blaizot J., Rosdahl J., 2015. eprint: arXiv:1510.06949, pp 105–108, http://adsabs.harvard.edu/abs/2015sf2a.conf..105T

Veilleux S., Cecil G., Bland-Hawthorn J., 2005, Annual Review of Astronomy and Astrophysics, 43, 769

Wise J. H., Cen R., 2009, ApJ, 693, 984

This paper has been typeset from a TEX/LATEX file prepared by the author.